# A fully distributed non linear waveguide using (Pb,Sr)TiO3 thin film : second and third harmonics generation

Freddy Ponchel, Ludovic Burgnies, D. Ducatteau, Eric Lheurette, Denis Remiens, D. Lippens

# A fully distributed non linear waveguide using (Pb,Sr)$TiO_3$ thin film: Second and third harmonics generation

Cite as: J. Appl. Phys. **114**, 194103 (2013); https://doi.org/10.1063/1.4831660
Submitted: 12 September 2013 • Accepted: 30 October 2013 • Published Online: 18 November 2013

F. Ponchel, L. Burgnies, D. Ducatteau, et al.



JOURNAL OF APPLIED PHYSICS **114**, 194103 (2013)

# A fully distributed non linear waveguide using (Pb,Sr)$TiO_3$ thin film: Second and third harmonics generation

F. Ponchel,[1,a)] L. Burgnies,[2,3] D. Ducatteau,[2] É. Lheurette,[2] D. Rémiens,[1] and D. Lippens[2]
[1]*Institute of Electronics, Microelectronics and Nanotechnology (IEMN)-DOAE Department, UMR CNRS 8520, Université de Valenciennes et du Hainaut Cambrésis, Le Mont Houy, 59313 Valenciennes cedex 9, France*
[2]*Institute of Electronics, Microelectronics and Nanotechnology (IEMN)-DHS Department, UMR CNRS 8520, Université des Sciences et Technologies de Lille, 59652 Villeneuve d'Ascq Cedex, France*
[3]*Université du Littoral Côte d'Opale, 62228 Calais cedex, France*

(Received 12 September 2013; accepted 30 October 2013; published online 18 November 2013)

We report on the experimental investigation of a non-linear (NL) Co-Planar Waveguide (CPW) fabricated by means of a ferroelectric film. In contrast to conventional NL-CPW, periodically loaded by lumped varactors, the tunable ferroelectric material is fully distributed along the propagation direction and the transmission line does not intrinsically exhibit Bragg cutoff. The experimental demonstration is carried out by means of a 160 nm-thick $Pb_{0.4}Sr_{0.6}TiO_3$ ferroelectric film voltage-controlled via the 1 $\mu$m-slot of a CPW transmission line. In a first stage, complex dielectric constant has been retrieved from scattering parameters measurements up to 60 GHz and for a bias voltage ranging from 0 to 30 V. High performances in terms of tunability have been found by a relative permittivity change under 30 V as high as 60% in the overall frequency band. Subsequently, the tunable ferroelectric CPW was used for second and third harmonics generation for a fundamental at centimeter wavelengths. While for low dc-voltage, third harmonic generation is dominant, it is found a main harmonic generation of rank 2 at higher dc bias voltage in agreement with the symmetry properties of the $C(V)$ characteristics. © *2013 AIP Publishing LLC*. [http://dx.doi.org/10.1063/1.4831660]

## I. INTRODUCTION

Voltage-controlled transmission lines are now attracting much interest with the prospect to realize tunable phase-shifter,[1,2] waveform shaper,[3] frequency multiplier,[4,5] or more generally nonlinear devices.[6–9] For tunability principle so far, the key technologies are based on the voltage-controlled capacitance of semiconductor[10,11] or ferroelectrics varactors[12,13] and MEMS technologies.[14,15] For the former by targeting RF/microwave applications, the periodically loading of a Co-Planar Waveguide (CPW) suitable for using surface mounting devices is a good trade-off between hybrid integration and performance. For an operation at higher frequencies and notably at millimeter wavelengths, ferroelectric thin film technology is generally preferred taking benefit of the recent progress in the achievement of high dielectric relaxation frequencies in the Terahertz frequency range.[16,17] Whereas ferroelectrics can be considered as a bulk technology in essence, the integration of discrete devices along the line, with close electrodes, appears necessary for preserving moderate voltage control. Indeed, the permittivity variation as a function of a dc or ac voltage intrinsically depends on the electric field across the active region which has to be higher than 100 kV/cm for the current ferroelectric technology.[18] Under this condition, it is imperative to downsize dramatically the electrodes spacing locally. In addition, for these periodically loaded transmission lines, the dimensions, such as the slot width, were kept to conventional values. For instance, the slot width of the CPW we used in Ref. 19 was $s = 30\ \mu$m, whereas the electrode inter-distance of the lumped inter-digitated varactors was 1 $\mu$m which enable the control under 30 V. On the other hand, it should emphasized that the decrease of the slot width which is beneficial for moderate voltage control or pumping is at the detriment of the ohmic losses due to the increased current crowding. As a consequence, there exists a trade-off between the controlling voltage reduction and loss considerations. Also, it is well known that periodically loading a transmission line results in the so-called Bragg frequency ($F_b$) cut-off. Such a cut-off intrinsically results from the multiple reflections of the travelling wave at each varactor position as it would be the case at each interfaces of an optical Bragg mirror. Shorter is the period between active elements, higher is the Bragg frequency so that ideally a distributed configuration has to be preferred for ultra wide band applications. If we compare the results reported here with the results published in the literature for CPW periodically loaded by varactors, it can be noticed that most of the works exhibit Bragg cut-off frequency generally in the upper part of the centimeter wavelengths.[5,19,20] In the present work, owing to a full distributed configuration no partial reflection occurs all along the transmission lines which was assessed by network analysis up 60 GHz. In counterpart, the major technological challenge of fully distributed CPW is the ability to deposit a long (millimeter size in the present work) CPW metal scheme with narrow slots on a micrometer scale here in order to get tunability at relative low dc voltage (tens of volts). This

[a)]Author to whom correspondence should be addressed. Electronic mail: freddy.ponchel@univ-valenciennes.fr.

 

dramatic down-sizing of the CPW slot can be also benefit for harmonic generation at moderate pumping voltage.

Unlike the solid state varactor diodes which can only be used under reverse bias, by excepting the so-called quantum barrier varactor,[21] ferroelectric-based varactors show similar $C(V)$ variations for reverse and forward bias voltages. At the inflexion point of the $C(V)$ characteristic, one can consider that the symmetry with respect to the bias voltage changes. Indeed, an even symmetry (equal values for direct and reverse biases) is pointed out around zero-Voltage. As a consequence, a dominant third harmonic generation is expected for unbiased device. In contrast around the voltage corresponding to the change of curvature, an odd symmetry is expected and hence a dominant second harmonic mode. As a consequence, it was predicted third and second harmonics generation by large signal analysis of ferroelectric transmission lines.[22] Also, some measurements confirmed the second harmonic occurrence under dc bias condition for a CPW fabricated with a slot of 10 $\mu$m.[22]

In this context, the contribution of the present paper is three fold. First, we report on the successful realization of a fully distributed nonlinear transmission line on the basis of the uniform deposition of a high quality $Pb_{0.4}Sr_{0.6}TiO_3$ ferroelectric film and the fabrication of a 1 $\mu$m-wide slot CPW. Second, the complex dielectric constant is retrieved from the scattering parameters which have been measured up to 67 GHz and for a bias voltage ranging from 0 to 30 V. At last, we report on the results of an experimental large signal analysis for various dc- and ac- voltages by paying attention on the role played by the symmetry conditions of the $C(V)$ characteristic.

Technologies and measurement setup which have been used for the fabrication and the characterization of the tunable ferroelectric CPW are detailed in Sec. II. Section III deals with the experimental retrieval of the dielectric function of $Pb_{0.4}Sr_{0.6}TiO_3$ films. The large signal experiment is reported in Sec. IV, while concluding remarks and prospects are summarized in Sec. V.

## II. DESIGN, TECHNOLOGIES, AND MEASUREMENT SETUP

### A. Design

Fig. 1 shows a schematic of the CPW transmission line, whose electromagnetic properties were studied under small- and large- signal conditions with two goals (i) the retrieval of the ferroelectric film dielectric function and (ii) the assessment of the non-linear properties under moderate pumping. It is worth-mentioning that the same structure is used for the two tasks with the following advantages. First, the complex permittivity is determined experimentally continuously over a broad band and not at certain resonant frequencies and over a relatively large area (typically $3 \times 10^3$ $\mu m^2$) of the ferroelectric film. Second, the experimental verification of the non-linearity is performed with the same device under test so that the uncertainties due to fabrication and notably during the ferroelectric deposition can be alleviated.

With respect to a conventional CPW transmission line, there are mainly two key differences. The first one is the use

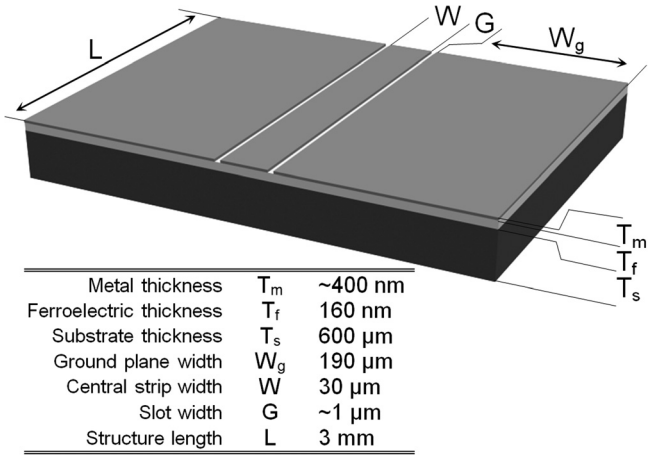


| | | |
|---|---|---|
| Metal thickness | $T_m$ | ~400 nm |
| Ferroelectric thickness | $T_f$ | 160 nm |
| Substrate thickness | $T_s$ | 600 µm |
| Ground plane width | $W_g$ | 190 µm |
| Central strip width | W | 30 µm |
| Slot width | G | ~1 µm |
| Structure length | L | 3 mm |

FIG. 1. Schematic view of Non-Linear Co-Planar Waveguide (NL-CPW).

of a voltage-controlled substrate with the realization of a bi-layered host wafer made of a 160 nm ultra-thin ferroelectric film and of a 600 $\mu$m-thick silicon wafer. Wave-guiding is achieved via 400 nm–thick metal strips, whose dimensions ($W_g$ and $W$) are listed in the inset of Fig. 1. The choice to use a relatively thick metal thickness is motivated by the reduction of ohmic losses. The other major difference is the dimension of the slot which is here 1 $\mu$m with the potential advantage of a dramatic reduction of the required pumping power and/or of the dc bias as outlined in the Introduction. It is worth mentioning that the central strip width was maintained to a conventional value typically 30 $\mu$m. With such a dimension, the design of a taper section between the test set-up using tip probes can be avoided. This makes easier the de-embedding of the set up environment and hence a much straightforward retrieval of the dielectric function. On the other hand, it will be seen that the transmission line is highly mismatched with respect to the reference impedance of the measurement set up ($Z_c = 50\ \Omega$).

For illustration of the operating conditions under ac excitation at a frequency of 10 GHz and a root mean square ac voltage $V_{rms} = 1$ V without dc biasing, Fig. 2 shows the snapshots of the magnitude of the electric field (a) and of the magnetic field (b) in a plane corresponding to the device cross-section in the vicinity of a slot. These electromagnetic field maps were computed by using an home-made code based on the two-dimensional finite element methods described in the article of Zoltan Cendes *et al.*[23] These methods were adapted especially for the material characterization at microwaves.[24]

Considering the electric field map carried out by assuming a constant permittivity of the ferroelectric film $\varepsilon_r = 360$, it can be noticed a high concentration of the electric field around the slot with a relatively isotropic decrease of the electric field magnitude in air and in the substrate. More importantly, high fringing field values can be seen in the tunable ferroelectric material with comparable magnitudes to those between the two 400 nm-thick electrodes. In addition, it can be noticed a relatively weak distortion of the electric field contours due to the 2 D implementing of the electrode. At last, edge effects are evidenced at the four corners of the metal plates with values which can be four time higher than

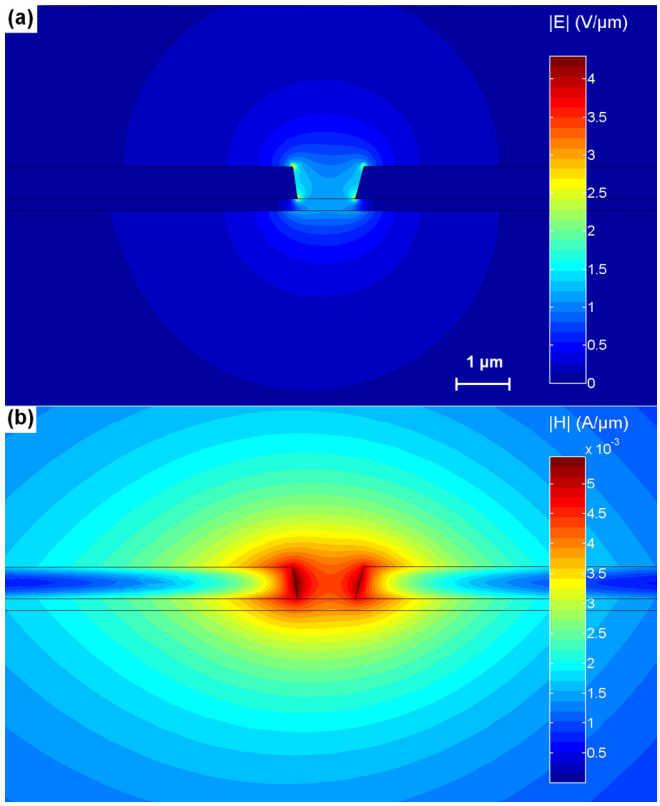


FIG. 2. Transverse electric field (a) and transverse magnetic field (b) computed from SEM view of tested CPW (Fig. 4) at $F = 10\,\text{GHz}$, $V_{dc} = 0\,\text{V}$, $V_{ac\text{-}rms} = 1\,\text{V}$, and $\varepsilon_{\text{r-PST}} = 360$.

the nominal values in the ferroelectric film. The field distribution is thus non uniform in the tunable layer, as expected. However, the electric peaks at the metal/dielectric boundaries vanish rapidly and the electric field can be considered with a relatively uniform value over the largest part of the tunable ferroelectric film. For a more quantitative estimate of the relative sharing of the field between the tunable material and its environment (air and semiconductor substrate), it can be suitable to compute the effective permittivity ($\varepsilon_{reff}$) of the CPW transmission line. For the present device, with a ferroelectric layer as thin as 160 nm and for a one-micron-wide slot, $\varepsilon_{reff} = 30$, but this value would dramatically decrease by enlarging the slot width.

Turning now to the magnetic field magnitude map displayed in Fig. 2(b), a high concentration of the field can be also pointed out in the vicinity of the slot. Such a concentration can be understood by reminding that the magnetic field lines wrap around the central strip. The H-field lines are thus more concentrated by crossing the ultra-narrow gap at the slot position. Also in our case, these effects are affected by the edge current repartition due to the ac operating conditions.

### B. Technologies (ferroelectric deposition and device fabrication)

Lead strontium titanate $Pb_{0.4}Sr_{0.6}TiO_3$ (PST) thin film was first deposited by radio frequency magnetron sputtering onto a High Resistivity Silicon substrate (HR-Si). On the basis of a previous material parametric study a Pb/Sr ratio of 40/60 was used in order to obtain a maximum value of the tunability. The Curie temperature (Tc) for a Pb/Sr ratio of 40/60 was estimated around 293 K by assuming a quasi linear variation between the Curie temperature of SrTiO3 ($Tc = 43\,\text{K}$) and PbTiO3 ($Tc = 760\,\text{K}$) taken from Ref. 25. Depositions were made *ex-situ* (without substrate heating during the growth) and a post-annealing treatment was necessary to crystallize the film in the Perovskite phase. Lei *et al.* showed that a pure Perovskite structure, without second phase, appears for an annealing temperature above $T = 450\,^{\circ}\text{C}$ with an optimal crystallization at $650\,^{\circ}\text{C}$.[26] For ferroelectric structural assessment, X-ray diffraction (XRD) was performed using a Siemens D5000 diffractometer. The scan covered the $2\theta$-range from 20° to 60° with a step of 0.02°. It revealed a polycrystalline film with a preferred (110) orientation as can be seen in Fig. 3. More details about the thin film preparation are given in Ref. 26. At this stage, it can be concluded that PST thin films present several advantages for fully distributed nonlinear-CPW, or more generally in any ferroelectric-based microwave agile devices. First, the PST layer used here was annealed at $650\,^{\circ}\text{C}$. This thermal budget is relatively low in comparison with the crystallization temperature of other ferroelectric films. In addition, the processing is compatible with Silicon Integrated Circuits technology. At last, a high tunability is obtained. In comparison to $BaSrTiO_3$ (BST) deposited on the same substrate an improvement of a factor 2 was measured on the tunability and of 3.35 on the figure of merit defined as of the product of tunability and quality factor.[13] For the definition of a figure of merit which was used for comparing PST and BST materials, we used Eq. (49) of Ref. 27

$$K = \frac{(n-1)^2}{n * tan\delta_1 * tan\delta_2}. \quad (1)$$

In this equation $n$ is the capacitance ratio ($C_1/C_2$) and $tan\delta_1$-$tan\delta_2$ the loss tangents between two switching states noted 1 and 2 in Ref. 27. In our case, the two states would

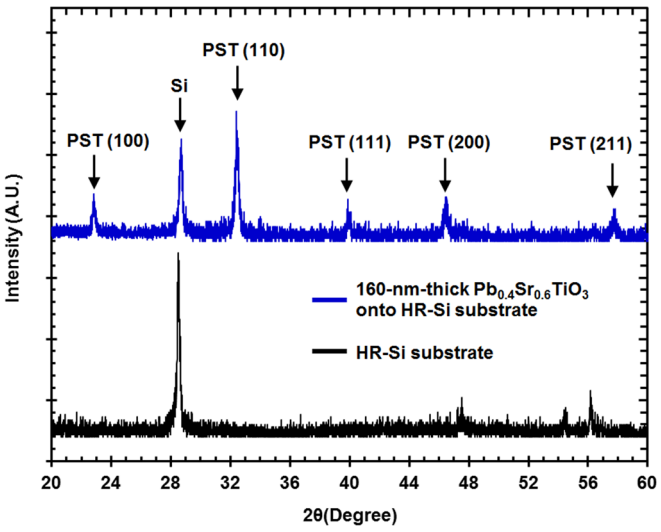


FIG. 3. X-ray diffraction patterns of PST film deposited on HR-Si substrate with a post annealing temperature of 650 °C. Black line: HR-Si substrate alone. Blue line: 160-nm-thick PST onto HR-Si substrate.

correspond to the values of the real part (capacitance ratio) and the imaginary part (loss tangent) of the complex permittivity under zero-volt and a voltage control of 30 V over 1 $\mu$m ($E_{dc} = 300$ kV/cm). Table I compares the BST and PST technologies developed in Ref. 28 and in the present work, respectively. As noted above $\varepsilon(0\text{ V})$ ($tan\delta(0\text{ V})$) and $\varepsilon(30\text{ V})$ ($tan\delta(30\text{ V})$) are the zero-bias permittivity (loss tangent) and the values which correspond to a dc bias field of 300 kV/cm.

From Table I, it can be noted that the figures of merit are close to $4.5 \times 10^3$ for PST and $1.5 \times 10^3$ for BST at a frequency of 5 GHz, the former value being comparable to the examples reported for a 5 GHz operation in Ref. 27 with $K = 5 \times 10^3$. As a general rule the figure of merit defined by Eq. (1) shows a decrease as a function of frequency due to the dramatic increase of the imaginary part of the complex permittivity and hence of loss tangent ($tan\delta(0\text{ V})$ and $tan\delta(30\text{ V})$). In addition, it can be noted that the $K$ values for BST are about three times higher than the one deduced for BST ferroelectric layers irrelevant of frequency up to 60 GHz. Therefore, PST is one of the most interesting materials available at present for applications where a maximum variation $\Delta\varepsilon/\Delta V_{dc}$ is sought.

For the device fabrication, the main technological challenge was the realization of the 1 $\mu$m slot over the 3 mm development of the CPW. This resolution is obtained by 365 nm UV photolithography techniques using an AZ® nLOF™ 2020 negative imaging photoresist and SUSS MicroTec MA/BA6 Mask Aligner. Planar electrodes consisting of a 50 nm Ti adhesion layer and 400 nm Au layer are deposited by PLASSYS MP550S electron beam evaporation system and subsequent lift-off. Fig. 4 shows a Scanning Electron Micrograph (SEM) of a typical device which confirms the cross-section dimensions.

### C. Measurement setups (small and large signal condition)

As seen in the following, the dielectric properties of the PST thin film were deduced from the scattering matrix of the HR-Si/PST/Au Co-Planar electrodes structure (Fig. 1) under small signal conditions. Scattering parameters were

TABLE I. Comparison of BST and PST technologies in term of $K$ factor (figure of merit) defined by Eq. (1).

| BST | | | | | |
|---|---|---|---|---|---|
| F (GHz) | $\varepsilon$ (0 V) | $\varepsilon$ (30 V) | $tan\delta$ (0 V) | $tan\delta$ (30 V) | $K$ |
| 5 | 299.52 | 198.65 | 0.021 | 0.006 | 1357.15 |
| 10 | 297.19 | 198.52 | 0.032 | 0.01 | 515.66 |
| 20 | 293.01 | 198.34 | 0.05 | 0.017 | 181.47 |
| 40 | 289.72 | 198.37 | 0.079 | 0.037 | 49.68 |
| 60 | 282.83 | 197.12 | 0.108 | 0.047 | 25.96 |
| **PST** | | | | | |
| F(GHz) | $\varepsilon$(0 V) | $\varepsilon$(30 v) | $tan\delta$(0 V) | $tan\delta$(30 V) | $K$ |
| 5 | 387.47 | 142.9 | 0.03 | 0.008 | 4501.16 |
| 10 | 382.78 | 145.51 | 0.054 | 0.011 | 1701.46 |
| 20 | 374.81 | 141.94 | 0.078 | 0.021 | 622.34 |
| 40 | 362.54 | 143,86 | 0.134 | 0.04 | 171.07 |
| 60 | 348.12 | 141.85 | 0.169 | 0.06 | 84.97 |

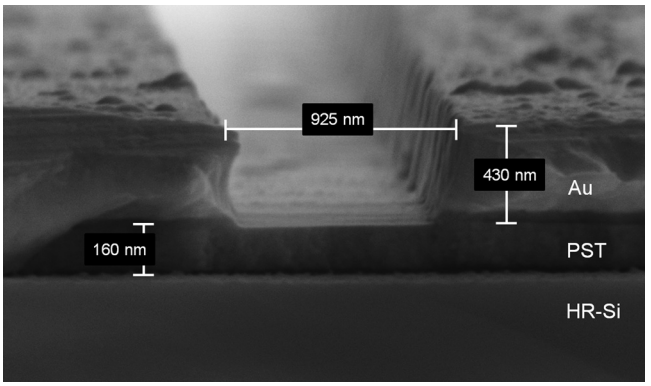


FIG. 4. Scanning Electron Micrograph (SEM) cross-section view of tested CPW.

measured from 0.25 GHz up to 60 GHz by means of an Agilent E8361A PNA microwave network analyser and a Cascade Microtech ground-signal-ground probe station. DC electric field was controlled by an Agilent E5263A 2-channel high speed source monitor unit. The measurement system was driven by IC-CAP device modeling software V2009. Each measurement was performed for an input power of 100 $\mu$W and the dc bias voltage is swept between +30 and −30 V with a step of 5 V. Under these conditions ($V_{dc} = 30$ V, $G = 1\ \mu$m), the nominal bias-field in the thin film is $E_{dc} = 300$ kV/cm.

Harmonic generation was assessed by a Large Signal Network Analyzer MT4463 from Maury Microwave. After a calibration process as described in Ref. 29, measurements were performed by supplying an incident wave $P_{ac}$ at port 1 for a fundamental frequency $F_0$ ranging from 1 GHz to 18 GHz, and by measuring harmonic generation up to rank 5 at ports 1 and 2. Port 2 is loaded by an impedance of $Z_L = 50\ \Omega$, and $P_{ac}$ is limited to 33.5 dBm (~2 W) to avoid the device burning out notably due to the field spikes evidenced in Sec. II A.

## III. COMPLEX DIELECTRIC FUNCTION

First, an exhaustive dielectric characterization, i.e., complex relative permittivity, loss tangent and tunability, was performed to obtain accurate small signal and dc behaviors of the ferroelectric PST film. As mentioned above, the method used to determine the dielectric properties of the unknown layer requires the scattering parameter measurement of the CPWs.

Each measurement was performed with a bandwidth of 10 Hz at the intermediate frequency of the vector network analyser in order to have a maximum dynamic range and hence a minimum transmission and reflection uncertainty (less than 0.2 dB for a dynamic range between 0 and −35 dB). This implies a relative uncertainty of approximately 2% on the thin film dielectrics properties results. Fig. 5 shows the measured [$S$]-parameters for seven $V_{dc}$ values ranging from 0 V up to 30 V. Fig. 5(a) and 5(b) display the frequency dependence of $S_{11}$ (return loss) at the input port and of $S_{21}$ (insertion loss). Return losses at port 2 ($S_{22}$, not represented here) and at port 1 were found very comparable. This condition $S_{11} = S_{22}$ ensures that the ferroelectric

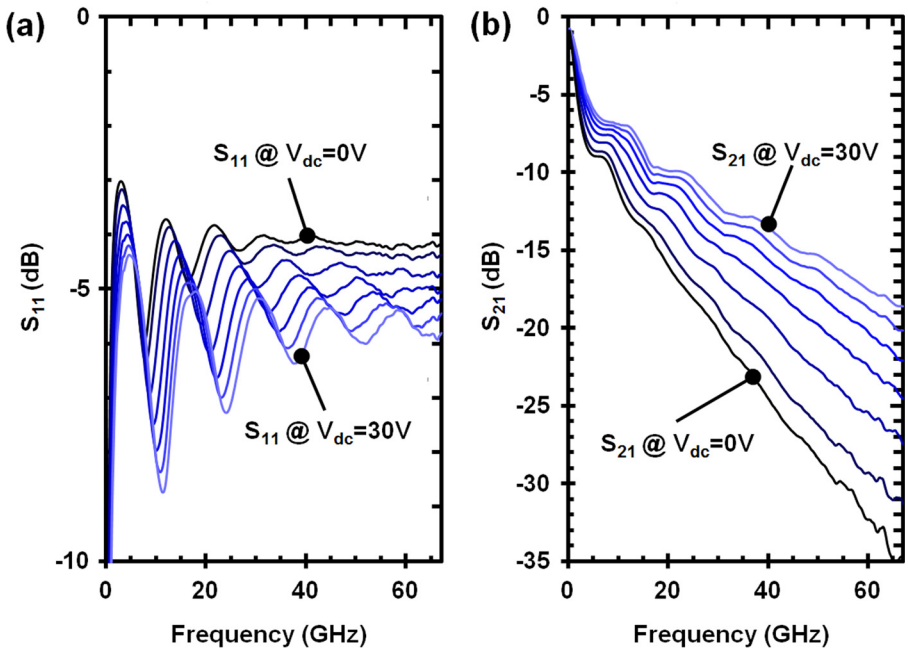


FIG. 5. Scattering parameters $S_{11}$ (a) and $S_{21}$ (b) of the ferroelectric CPW for dc bias voltage $V_{dc}$ varying from 0 to 30 V by step of 5 V.

layer underneath the electrode waveguide has a constant thickness. As a general rule for each $V_{dc}$, it can be noticed that the average value of $S_{11}$ over the frequency band is almost constant. Indeed, the oscillating features, apparent on the frequency variations, result from the impedance mismatch at the input and output ports with resonance conditions depending on the CPW length (here 3 mm). In addition, it can be noted that the $S_{11}$ extrema are shifted toward higher frequency with increasing bias voltage, indirectly assessing the decrease of the effective permittivity.

From these measured [S]-parameters, and from an accurate determination of the topology and dimensions obtained by SEM imaging, the dielectric characteristics were retrieved numerically by means of the home made full electromagnetic software introduced in Sec. II A. At each frequency, the numerical procedure for the retrieval of the dielectric function of the ferroelectric layer is based on a comparison of measured and computed [S]-matrixes. The S parameters are calculated numerically by using the classical equations which relate the $S_{ij}$ terms to the current, voltage, characteristic impedance ($Z_c$) and propagation constant ($\gamma = \alpha + j\beta$) which characterize the transmission lines.[30] Voltage and current are deduced by proper integration of field maps. By an iterative process similar to the Newton-Raphson method working in a 4-axis graph ($\alpha$, $\beta$, $\varepsilon'$, $\varepsilon''$), a new complex permittivity is assigned to the dielectric layer under test yielding a new value of [S]-matrix which is compared again with the measured one. After convergence, the complex permittivity ($\varepsilon^* = \varepsilon' - \mathrm{j}\,\varepsilon''$) of the PST layer for every frequency and each $V_{dc}$ bias voltage is thus retrieved. The frequency dependences of $\varepsilon'$ and $\varepsilon''$ are shown in Fig. 6(a) while loss tangent ($tan\delta = \varepsilon''/\varepsilon'$) is plotted in Fig. 6(b). The oscillatory features

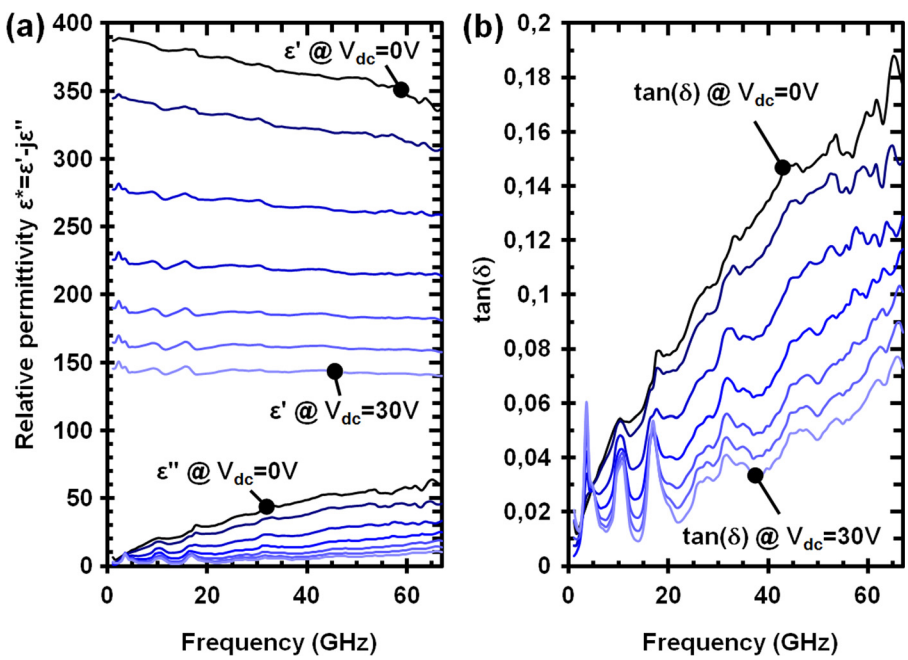


FIG. 6. Complex permittivity $\varepsilon^* = \varepsilon' - j\,\varepsilon''$(a) and loss tangent (b) for dc bias voltage $V_{dc}$ varying from 0 to 30 V by steps of 5 V.

in the frequency dependence of loss tangent are a direct consequence of very weak anomalies which are apparent by zooming the frequency dependence of the scattering parameters around 4, 10, and 17 GHz, respectively. With respect to the physical interpretation, as in our previous work[31] reporting on such singular effects, these anomalies in the frequency dependence of loss tangent were explained by electrostriction and piezoelectric effect[32] and more particularly by acoustic wave resonances. A model that explains this particular effect has been developed by Lakin *et al.*[33] From the frequency dependence of the real part $\varepsilon'$, it can be noticed a slight decrease versus frequency at zero volt, whereas the values are almost constant at $V_{dc} = 30$ V. The physical interpretation of such a decrease of the observed slope, depending on the bias voltage, in terms of relaxation phenomena is beyond the scope of the present work. However, it was shown that these effects can be explained by a shift of the Curie temperature to higher temperatures.[18]

To sum up, one can conclude that voltage-controlled high permittivity values (of the order of 350) slightly varying with frequency have been demonstrated experimentally over a broad frequency band (in practice from 0.25 to 67 GHz). From Fig. 6(a), one can also note that the losses ($\varepsilon''$) are improved with increasing bias voltage as already pointed out in the frequency dependence of $S_{21}$ (Fig. 5(b)). For completeness in the material data, Fig. 6(b) shows the frequency dependence of loss tangent with a worst value of 18% for zero bias and a best value of 6% at $V_{dc} = 30$ V recorded at 60 GHz.

Turning now to the capacitance voltage characteristic taking the frequency as a parameter, we plotted in Fig. 7 the real part of the relative permittivity retrieved for $F = 5$ GHz and 60 GHz respectively. For $F = 5$ GHz, a high tunability $T = [\varepsilon'(0\,V) - \varepsilon'(V_{dc})]/\varepsilon'(0\,V)$ of 63% (43%) is measured for $V_{dc} = 30$ V (16 V). At higher frequencies, tunability is slightly degraded with a value of 59% at 60 GHz. To the best of our knowledge, these values can be considered as record performances for PST thin-film deposited in a silicon compatible technology. They also comparable favorably with respect to those reported for BST films.[31]

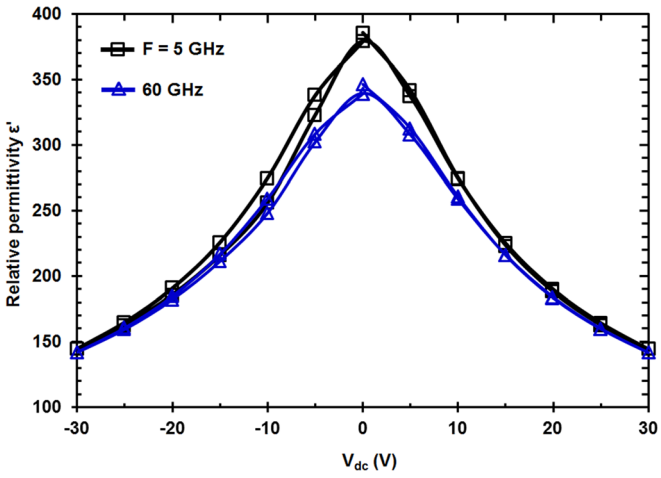


FIG. 7. Real part of relative permittivity versus $V_{dc}$ measured for $F = 5$ GHz and 60 GHz.

## IV. NON LINEAR ANALYSIS

Symmetric curves in Fig. 7 with even parity without any butterfly-shape result from the ferroelectric material in paraelectric phase at room temperature. From $\varepsilon(V)$ characteristic, odd harmonic generation is expected for a large ac signal around $V_{dc} = 0$ V, and even harmonic generation around the inflection point at $V_{dc} = 10$ V. Harmonic generation was measured at port 1 and at port 2 as a function of the dc bias voltage $V_{dc}$ from 0 V to 16 V, and for a power of the incident wave $P_{ac}$ taken as a parameter varying up to 33.5 dBm. Fig. 8 shows a spectral decomposition of the harmonic generation measured at port 1 and port 2 for $P_{ac} = 33.5$ dBm and a fundamental frequency $F_0 = 1$ GHz. For $V_{dc} > 2$ V, second harmonic ($m = 2$) is mainly generated with a maximum of 8.6 dBm and 6.9 dBm at port 1 and port 2, respectively, for $V_{dc} = 11$ V. The same behavior is observed for $m = 4$ with a maximum generated at lower $V_{dc} = 4.5$ V with three orders of magnitude lower than $m = 2$. The third harmonic generation is maximum for $V_{dc} = 0$ V and decreases with $V_{dc}$ reaching a minimum value at $V_{dc} = 10$ V at port 2. The fifth harmonic level is too low and cannot be interpreted. Except for second harmonic generation, all power levels at port 2 are greater than levels at port 1. However, as shown latter, no conclusion can be made because harmonic levels at port 1 and 2 depend on the fundamental frequency as well. All curves are in good agreement with the parity of the $\varepsilon(V)$ characteristic plotted in Fig. 7 with third harmonic generated at low dc and higher even harmonic under dc bias. Results can be synthesized by plotting the total power generated in CPW versus $V_{dc}$ as shown in Fig. 9. Total power is calculated as

$$P_T(P_{ac}) = \sum_{m=1,2,\ldots} PH_m(P_{ac}), \tag{2}$$

where $PH_m$ represents the power of harmonic m measured at port 1 or port 2 for a power $P_{ac}$ of incident wave injected in port 1 and hence by taken the reflected power into account. Observing the results in Fig. 9, where each curve includes the contribution of all harmonics in accordance with Eq. (2), we can see a predominant second harmonic generation for all $P_{ac}$ values around $V_{dc} = 10$ V. Below $P_{ac} = 26.4$ dBm, harmonic generation is split into equal parts to port 1 and port 2. Also, the power of the third harmonic below $-35$ dBm is too low to be detected, and only the second harmonic generation is measured. At higher power, harmonics are slightly more generated at port 1 than at port 2, while at low dc bias third harmonic generation at port 2 increases the total generated power reducing the overall variation of $P_T$. That can be attributed to the frequency dependence of losses and characteristic impedance of the line. As shown in Fig. 5(b), the attenuation constant of CPW increases with frequency, and harmonics of higher ranks are more attenuated. On the other hand, the permittivity-voltage dependence of the PST plotted in Fig. 7 results in an increase of characteristic impedance of the line under bias.[31] More precisely, dielectric losses and impedance mismatch decrease with increasing $V_{dc}$ and increase with the frequency. As observed in Fig. 8, it results a more favorable conditions for second

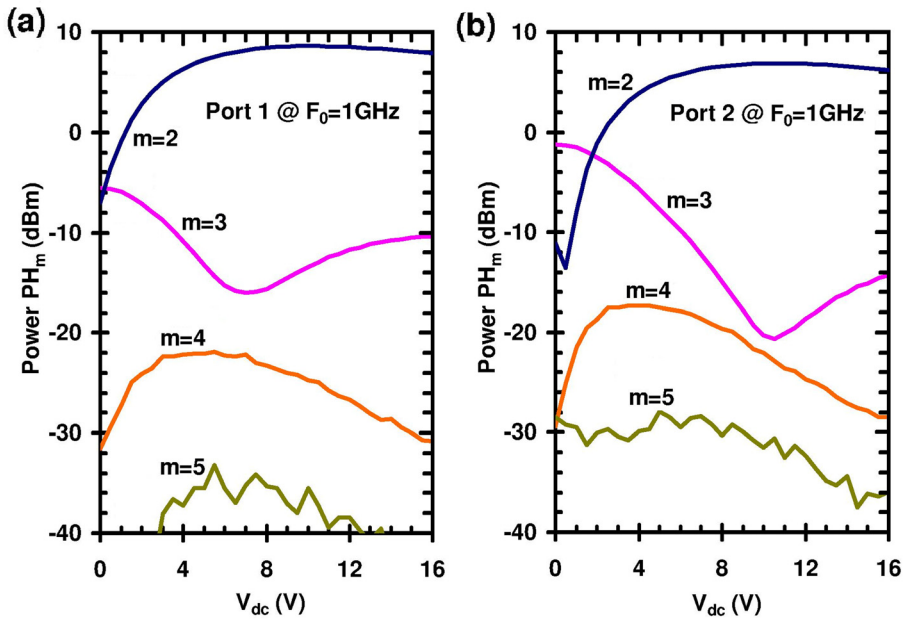


FIG. 8. Spectral decomposition of harmonic generation versus dc bias voltage measured at port 1 (a) and at port 2 (b).

harmonic generation, with lower propagation losses and lower impedance mismatch, than for higher ones. Higher levels of harmonics measured at port 2 (around +2 dBm comparatively to port 1) can also be attributed to the highest attenuation at higher frequency. For $m \geq 3$, harmonics measured at port 2 mainly correspond to forward waves generated near the port 2, while reflected harmonic waves by impedance mismatch at port 2 are strongly attenuated by CPW losses before to reach port 1. On the other hand, for the second harmonic, attenuation constant is lower and the reflected harmonic waves can contribute to the overall harmonic generation measured at port 1.

In Fig. 10, maxima of the total generated power $P_T$ versus power of incident wave $P_{ac}$ measured at various fundamental frequencies $F_0$ are plotted. For each $P_{ac}$, dc bias voltage has to be adjusted to obtain the maximum of $P_T$. As evidenced in Fig. 9, maxima of $P_T$ are determined at different dc bias voltage ranging from $V_{dc} = 8.5$ V for $P_{ac} = 20.4$ dBm up to 11 V for 33.5 dBm. For each frequency in Fig. 10, maximum of $P_T$ is linearly dependent of $P_{ac}$ with a slope of 2 and without any saturation effect at high $P_{ac}$. As previously pointed out by Rocas *et al.*,[22] a slope 2 corresponds to a main second harmonic generation in good agreement with the decomposition of harmonics shown in Fig. 8. At port 2, maximum of $P_T$ decreases with the fundamental frequency and a plateau is reached above $F_0 = 10$ GHz. On the contrary at port 1, maximum of $P_T$ strongly decreases for 4 GHz before to increase for 10 GHz, and again to decrease for 18 GHz. For higher frequencies, standing waves take place in CPW line. Around $F = 5$ GHz, wavelength in the CPW is 12 mm, and a voltage node appears at the end of the line. For $F = 10$ GHz, the voltage node is placed in the middle of the line, and for 18 GHz there are two voltage modes along the line. To the best of our knowledge, the number of

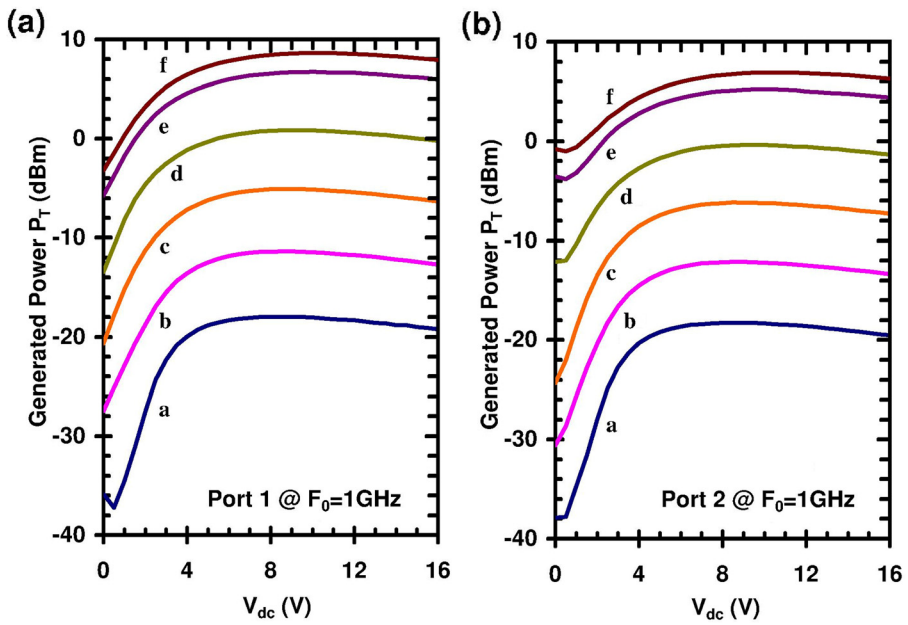


FIG. 9. Total power as a function of dc bias voltage measured at port 1 (a) and at port 2 (b) for a fundamental frequency $F_0 = 1$ GHz, and for $P_{ac} = 20.4$ dBm (a), 23.4 dBm (b), 26.4 dBm (c), 29.4 dBm (d), 32.5 dBm (e), and 33.5 dBm (f).

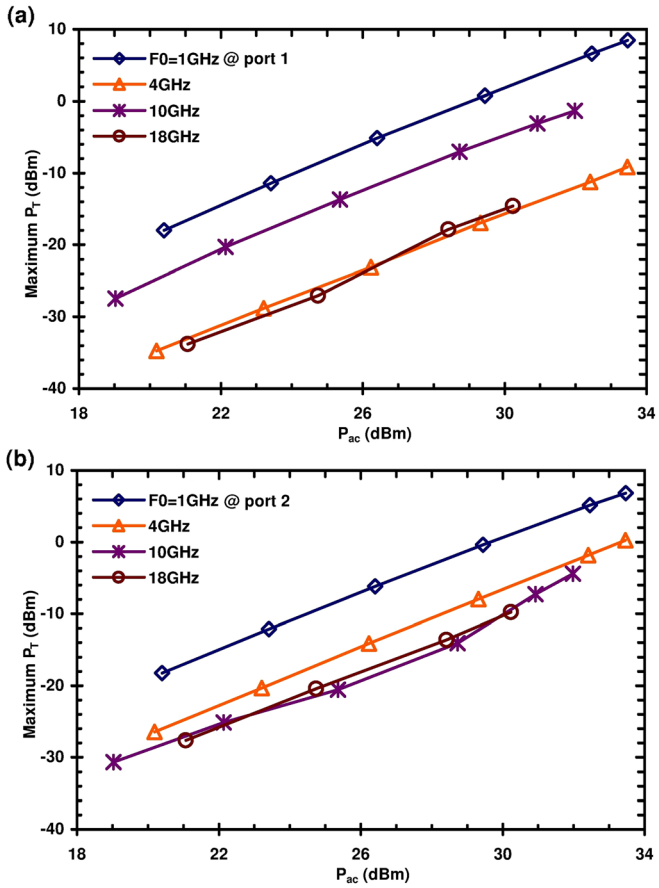


FIG. 10. Maximum of the total generated power measured at port 1 (a), and at port 2 (b) versus power of incident wave with various fundamental frequency $F_0$ as a parameter.

papers addressing nonlinear effects in fully distributed is scarce with periodically loaded transmission line. One of the most recent paper was published by Rocas *et al.* with an experimental verification on CPW with a 30 $\mu$m slot width and hence one order of magnitude larger than the one used in the present work. Second harmonic generation by ferroelectric CPW was pointed out by the authors[22] for an incident power less than 20 dBm at 6 GHz and with a conversion loss of 70 dB. In the present work, we showed that the conversion efficiency can be significantly improved (34 dB of conversion loss for the highest input power of 33 dBm) with respect to this previous work by taking benefit of the full non linearity owing to the dramatic decrease of the slot width. As aforementioned in Sec. II, the CPW studied in the present configuration here is strongly mismatched and therefore its overall performance in terms of conversion efficiency cannot be compared with impedance matched periodically loaded transmission. It is worth-mentioning that these conventional approaches exhibit frequency limitations such as in the paper published recently by Huang *et al.*, in 2011 who reported a decrease of the output power above 30 GHz.[5] Moreover, saturation effect does not appear at high power level in Fig 10, while harmonic generation could be limited for CPW loaded by varactors.[20]

For $F_0 = 4$ GHz, fundamental ac voltage is very low near the port 2 and little or no harmonic signal is generated at the end of the CPW line. In such a case, second harmonic measured at port 2 corresponds to the forward waves generated near the port 1. Forward waves are partly reflected at port 2 before to return at port 1 with destructive interferences giving a lower level of the generated power at port 1. For higher frequency, a more complex formulation has to be performed to better analyze harmonic generation with multiple standing waves and node voltages along the line. However, Fig. 10 shows that the power level of the second harmonic measured at port 1 can be greater at higher frequency. We assume that a same behavior could be measured at port 2 depending on the length of CPW line and fundamental frequency.[7] Finally, harmonic generation does not disappear at higher frequency and for $F_0 = 18$ GHz a power level of $-9.8$ dBm is measured.

## V. CONCLUSION

A one-micron slot 3 mm-long CPW pattern was successfully deposited onto a bi-layered PST ferroelectric/silicon structure. The retrieval of the complex permittivity under small signal conditions shows high values of the real part of the permittivity ($\varepsilon_r \sim 360$) and moderate dielectric loss up to 67 GHz. These films also show a high tunabilty around 60% which compare favorably with the previous results reported in the literature notably with respect to BST technologies. The high tunability is preserved in the upper part of the frequency band which was investigated, a welcome feature for a potential application as a fully distributed non-linear device operating at millimeter waves. Harmonics generation was thus demonstrated under moderate pumping results from the ultra narrow slot width up to a fundamental frequency $F_0 = 18$ GHz. For these non-linear experiments under dc bias, a predominant second harmonic generation was observed. Generated power is linearly dependent on the power $P_{ac}$ with a slope 2, and no saturation effect is observed. Finally, at high frequency when multiple standing waves take place in the CPW, maximum of power can be generated at port 1 or at port 2 depending on the fundamental frequency $F_0$ and the length of the line.

## ACKNOWLEDGMENTS

The authors appreciate the PST parametric study and fabrication efforts of X. Lei.[26] This work has benefited of the facilities of ExCELSiOR -Nanoscience Characterization Center and of the cleaning rooms of IEMN which is also one of the large technological facilities of the RENATECH national network.

[1]J. H. Leach, H. Liu, V. Avrutin, E. Rowe, Ü. Özgür, H. Morkoç, Y.-Y. Song, and M. Wu, J. Appl. Phys. **108**, 064106 (2010).
[2]S. Sheng, P. Wang, X. Chen, X.-Y. Zhang, and C. K. Ong, J. Appl. Phys. **105**, 114509 (2009).
[3]Q. R. Marksteiner, B. Carlsten, and S. Russell, J. Appl. Phys. **106**, 113306 (2009).
[4]M. Dragoman, D. Neculoiu, G. Deligeorgis, G. Konstantinidis, D. Dragoman, A. Cismaru, A. A. Muller, and R. Plana, Appl. Phys. Lett. **97**, 093101 (2010).
[5]J. Huang, J.-R. Dong, H. Yang, H.-Y. Zhang, C. Tian, and T.-Y. Guo, Chin. Phys. B **20**(6), 060702 (2011).
[6]A. Findikoglu, R. Camassa, G. Lythe, and Q. X. Jia, Appl. Phys. Lett. **80**, 3391–3393 (2002).

[7]T. B. Samoilova, K. F. Astafiev, T. Rivkin, and D. S. Ginley, J. Appl. Phys. **90**(11), 5703–5707 (2001).
[8]A. Deleniv, P. Rundqvist, A. Vorobiev, E. Kollberg, and S. Gevorgian, IEEE-MTT-S International Microwave Symposium (2007).
[9]M. G. Case, Ph.D. dissertation, Elect. Comput. Eng. Dept., Univ. California at Santa Barbara, Santa Barbara, CA, 1993.
[10]W. Xu and S. Sonkusale, Appl. Phys. Lett. **103**, 031902 (2013).
[11]Z. Wang, Y. Luo, L. Peng, J. Huangfu, T. Jiang, D. Wang, H. Chen, and L. Ran, Appl. Phys. Lett. **94**, 134102 (2009).
[12]M.-G. Kang, K.-H. Cho, Y. Ho Do, Y.-J. Lee, S. Nahm, S.-J. Yoon, and C.-Y. Kang, Appl. Phys. Lett. **101**, 242910 (2012).
[13]A. Marteau, G. Velu, G. Houzet, L. Burgnies, E. Lheurette, J. C. Carru, and D. Lippens, Appl. Phys. Lett. **94**, 023507 (2009).
[14]Y.-S. Lin, Y. Qian, F. Ma, Z. Liu, P. Kropelnicki, and C. Lee, Appl. Phys. Lett. **102**, 111908 (2013).
[15]Y. Shim, Z. Wu, and M. Rais-Zadeh, IEEE Trans. Microwave Theory Tech. **60**(8), 2439–2447 (2012).
[16]G. Houzet, L. Burgnies, G. Velu, J.-C. Carru, and D. Lippens, Appl. Phys. Lett. **93**, 053507 (2008).
[17]G. Houzet, K. Blary, S. Lepilliet, D. Lippens, L. Burgnies, G. Vélu, J. C. Carru, E. Nguéma, and P. Mounaix, Ferroelectrics **430**(1), 36–41 (2012).
[18]S. Gevorgian, *Ferroelectrics in Microwave Devices, Circuits and Systems* (Springer, London, 2009).
[19]G. Vélu, K. Blary, L. Burgnies, A. Marteau, G. Houzet, D. Lippens, and J. C. Carru, IEEE Trans. Microwave Theory Tech. **55**(2), 438–444 (2007).
[20]J. Huang, J. Dong, H. Yang, H. Zhang, C. Tian, and T. Guo, Trans. Microwave Theory Tech. **59**(10), 2486–2493 (2011).
[21]M. Fernandez, E. Delos, X. Mélique, S. Arscott, and D. Lippens, IEEE Microw. Wirel. Compon. Lett. **11**(12), 498–500 (2001).
[22]E. Rocas, C. Collado, J. Mateu, N. Orloff, J. M. O'Callaghan, and J. C. Booth, IEEE Trans. Microwave Theory Tech. **59**(12), 3059–3067 (2011).
[23]Z. J. Cendes, IEEE Trans. Magn. **27**, 3958–3966 (1991).
[24]F. Ponchel, Ph.D. dissertation N°4077, University of Lille, 2007.
[25]T. Fujii, J. Du, T. Karaki, and M. Adachi, J. Korean Phys. Soc. **42**, 1178–1181 (2003), available at http://www.kps.or.kr/home/kor/journal/library/downloadPdf.asp?articleuid=%7B6FC2F0A8-4F4F-4864-A4A6-DD5BE1013901%7D.
[26]X. Lei, D. Rémiens, F. Ponchel, C. Soyer, G. Wang, and X. Dong, J. Am. Ceram. Soc. **94**, 4323–4328 (2011).
[27]I. B. Vendik, E. L. Kollberg, and O. G. Vendik, Trans. Microwave Theory Tech. **48**(5), 802–808, (2000).
[28]F. Ponchel, J. F. Legier, C. Soyer, D. Remiens, J. Midy, T. Lasri, and G. Guéguan, Appl. Phys. Lett. **96**, 252906 (2010).
[29]D. Ducatteau, M. Werquin, B. Grimbert, E. Morvan, D. Theron, and C. Gaquiere, Proc. IEEE Instrum. Meas. Technol. Conf., pp.1–5 (2007).
[30]R. E. Collin, *Foundations for Microwave Engineering*, 2nd ed. (IEEE Press, Wiley, 2001).
[31]F. Ponchel, X. Lei, D. Rémiens, G. Wang, and X. Dong, Appl. Phys. Lett. **99**, 172905 (2011).
[32]S. Tappe, U. Böttger, and R. Waser, Appl. Phys. Lett. **85**, 624 (2004).
[33]K. M. Lakin, G. R. Kline, and K. T. McCarron, IEEE Trans. Microwave Theory Tech. **43**, 2933 (1995).